

CN and HCN in Dense Interstellar Clouds

Gai I. Boger and Amiel Sternberg

*School of Physics and Astronomy and the Wise Observatory, The Beverly and Raymond
Sackler Faculty of Exact Sciences, Tel Aviv University, Tel Aviv 69978, Israel*

amiel@wise.tau.ac.il

ABSTRACT

We present a theoretical investigation of CN and HCN molecule formation in dense interstellar clouds. We study the gas-phase CN and HCN production efficiencies from the outer photon-dominated regions (PDRs) into the opaque cosmic-ray dominated cores. We calculate the equilibrium densities of CN and HCN, and of the associated species C^+ , C, and CO, as functions of the far-ultraviolet (FUV) optical depth. We consider isothermal gas at 50 K, with hydrogen particle densities from 10^2 to 10^6 cm^{-3} . We study clouds that are exposed to FUV fields with intensities (at 1000 Å) from 5×10^{-19} to 5×10^{-14} $\text{erg s}^{-1} \text{cm}^{-2} \text{Hz sr}^{-1}$, or 20 to 2×10^5 times the mean interstellar FUV intensity. We assume cosmic-ray H_2 ionization rates ranging from $5 \times 10^{-17} \text{ s}^{-1}$, to an enhanced value of $5 \times 10^{-16} \text{ s}^{-1}$. We also examine the sensitivity of the density profiles to the gas-phase sulfur abundance.

Subject headings: galaxies:ISM – ISM:evolution – molecular processes

1. Introduction

Millimeter-wave line emissions of CN and HCN molecules are widely used probes of dense molecular gas and of photon-dominated regions (PDRs) in the Galactic interstellar medium (ISM). Observed sources include molecular interfaces in star-forming regions (Greaves & Church 1996; Simon et al. 1997; Young Owl et al. 2000; Savage et al. 2002; Schneider et al. 2003; Johnstone et al. 2003), reflection nebulae (Fuente et al. 1993, 1995, 2003; Jansen et al. 1995), planetary nebulae (Bachiller et al. 1997a), and circumstellar envelopes and disks (Wooten et al. 1982; Truong-Bach et al. 1987; Bachiller et al. 1997b; Lindqvist et al. 2000; van Zadelhoff et al. 2003; Thi et al. 2004). Observations of CN and HCN have recently been used to study PDRs in the starburst galaxy M82 and in other external systems (Fuente et al. 2005; Meier & Turner 2005).

In nearby objects, such as the Orion Bar and the reflection nebulae NGC 2023 and 7023, the molecular emissions have been mapped across the PDRs. The CN/HCN intensity ratios are largest near the stellar sources of the illuminating far-ultraviolet (FUV) radiation fields, and the intensity and density ratios decrease with increasing optical depth and distance from the stars. This behavior is broadly consistent with theoretical expectations (Sternberg & Dalgarno 1995 [SD95]; Jansen et al. 1995) and is evidence of selective photodissociation of HCN versus CN (van Zadelhoff et al. 2003; Thi et al. 2004).

Many discussions of gas-phase nitrogen chemistry in molecular clouds have been presented in the literature (e.g., Herbst & Klemperer 1973; Prasad & Huntress 1980; Viala 1986; Pineau des Forets et al. 1990; Herbst et al. 1994; SD95; Lee et al. 1996; Turner et al. 1997). Comprehensive reviews of PDR observations and theory, and related subjects have been presented by Hollenbach & Tielens (1999), Sternberg (2004), and van Dishoeck (2005).

In this paper we focus on the gas-phase production of CN and HCN, and present results for a wide range of conditions. We analyze how the CN and HCN formation and destruction sequences vary with optical depth, first through the PDRs and then into the opaque cosmic-ray dominated cores. We discuss how the (equilibrium) density profiles depend on the cloud hydrogen gas densities and the incident FUV field intensities, and we identify the qualitative changes in the density profiles that may be expected in moving from low- to high-density systems. The production efficiencies of the carbon bearing CN and HCN molecules depend on the availability of free C^+ ions and C atoms in the gas, and we present and discuss the associated C^+ , C, and CO density profiles in the parameter space we consider. In this paper we do not consider HNC or the isomeric abundance ratio HCN/HNC (e.g., Watson 1974; Schilke et al. 1992; Herbst et al. 2000) which, together with CN/HCN, may be expected to vary with optical depth, density, and FUV field strength.

In §2 we describe the basic ingredients of our models. In §3 we discuss the gas-phase CN and HCN reaction sequences that operate in molecular clouds. In §4 we present detailed results for a “reference model” to illustrate the depth-dependent formation pathways and density profiles. In §5 we present our parameter study and discuss results for a range of gas densities, FUV field strengths, cosmic-ray ionization rates, and gas-phase elemental abundances. We summarize in §6.

2. Model Ingredients

We performed our model computations using an updated version of the SD95 code. The models consist of static, plane-parallel, semi-infinite slabs, exposed on one side to isotropic

FUV (6-13.6 eV) radiation fields. The steady-state abundances of the atomic and molecular species are computed as functions of the visual extinction, A_V , from the cloud surface. The models account for scattering and absorption of the FUV photons by dust grains, and the resulting depth-dependent attenuation of the atomic and molecular photodissociation and photoionization rates. The effects of H_2 and CO absorption-line shielding are also included. The molecular chemistry is driven by the combined action of FUV photoionization and photodissociation, and cosmic-ray impact ionization. The resulting sequences of (two-body) gas-phase ion-molecule and neutral-neutral reactions are mediated by dissociative recombination and photo-destruction.

We assume that the spectral shapes of the incident FUV fields are identical to the Draine (1978) representation of the interstellar field in the solar neighborhood (see also Parravano, Hollenbach & McKee 2003). The field intensity is parameterized by a scaling factor χ , where for $\chi = 1$ the FUV intensity at 1000 Å is 5.4×10^{-20} erg s $^{-1}$ cm $^{-2}$ Hz $^{-1}$ sr $^{-1}$. We construct models for χ ranging from 20 to 2×10^5 , appropriate for PDRs in the vicinity of young OB stars and clusters (Sternberg et al. 2003).

In our computations we include the same set of 70 atomic and molecular carbon, nitrogen, oxygen, sulfur, and silicon bearing species¹ considered by SD95. Complex hydrocarbons and PAHs are excluded. We solve the depth dependent equations of chemical equilibrium

$$\sum_{jl} k_{ijl}(T)n_j n_l + \sum_j [\chi\Gamma_{ij} + \xi_{ij}]n_j = n_i \left\{ \sum_{jl} k_{jil}n_l + \sum_j [\chi\Gamma_{ji} + \xi_{ji}] \right\} \quad (1)$$

as functions of A_V . In these equations, n_i are the densities (cm $^{-3}$) of species i , and $k_{ijl}(T)$ are the (temperature-dependent) rate coefficients (cm 3 s $^{-1}$) for chemical reactions between species j and l that lead to the production of i . The parameters $\chi\Gamma_{ij}$ and ξ_{ij} are the FUV photon and cosmic-ray destruction rates (s $^{-1}$) of species j with products i . We solve Equations (1) via Newton-Raphson iteration, and use Bulirsch-Stoer integration to compute the column densities.

In our computations we include all reactions listed in the UMIST99 database (Le Teuff et al. 2000) for which the reactants and products are species in our set. We adopt the recommended UMIST99 rate-coefficients k_{ijl} , with several alterations and updates².

¹We assume that the abundances of all other elements are negligible in the gas phase, including heavy elements such as Mg and Fe which, when abundant, may become important positive-charge carriers in dense molecular clouds (Oppenheimer & Dalgarno 1974; de Boisanger et al. 1996).

²Our input list of rate coefficients is available at <ftp://wise3.tau.ac.il/pub/amiel/pdr>. In our compilation we use recent determinations of the rate coefficients and branching ratios for dissociative recombinations

The depth-dependent FUV photodissociation and photoionization rates are crucial quantities. They depend on the intensity and spectral shape of the incident radiation field, on the photodissociation and photoionization cross-sections, and on the dust grain scattering and absorption properties. Dust attenuation is the primary mechanism for the reduction of the photorates. Line-shielding is also important for the special cases of H₂ and CO photodissociation³. For the depth dependent photodissociation and photoionization rates, we adopt the biexponential representations

$$\Gamma_i = C_i \exp(-\alpha_i A_V - \beta_i A_V^2) \quad (2)$$

and coefficients, C_i , α_i , and β_i , calculated by SD95 for the radiative transfer of a Draine field penetrating a cloud of large ($A_{Vtot} = 100$) total optical depth (Roberge et al. 1991). We assume a dust-to-gas ratio such that $A_V = 4.75 \times 10^{-22} (N_H + 2N_{H_2})$ (SD95; see also Draine 2003) where N_H and N_{H_2} are the atomic and molecular hydrogen column densities (cm^{-2}). In Figure 1 we plot the CN and HCN photodissociation rates as functions of A_V , for $\chi = 1$ and a total cloud thickness $A_{Vtot} = 100$. The much more rapid attenuation of the CN photodissociation rate compared to HCN is an important feature of the models, and reflects the fact that the energetic photons (> 12.4 eV) required to dissociate CN (van Dishoeck 1987; Thi et al. 2004) are more readily absorbed by the dust grains.

The cosmic-ray destruction rates ξ_{ij} in equation (1) include impact ionizations of H, H₂ and He, by the primary cosmic-rays and secondary electrons, and induced FUV photodissociation and photoionization of the heavier molecules (Gredel et al. 1989). In most of our models we adopt a “dense cloud” H₂ cosmic-ray ionization rate, $\zeta = 5 \times 10^{-17} \text{ s}^{-1}$ (e.g., Williams et al. 1998), but we also examine the effect of increasing ζ by up to a factor 10 (McCall et al. 2003; Brittain et al. 2004). The cosmic-rays are “freely penetrating” and ζ is independent of cloud depth. Cosmic-ray ionization is the only source of H⁺, H₂⁺, and He⁺ in our models. X-ray ionization (Maloney et al. 1996; Spaans & Meijerink 2005) is excluded.

The cosmic-ray induced photoionization and photodissociation rates are given by

$$\xi_i = \frac{\zeta p_i}{1 - \omega} \quad (3)$$

(Vejby-Christensen et al. 1997; Larson et al. 1998; Vikor et al. 1999; Jensen et al. 2000; McCall et al. 2003; Geppert et al. 2004). For some neutral-neutral reactions we use rate-coefficients listed in UMIST95, or as given by Herbst et al. (2000) and Smith et al. (2004). We do not assume the small (~ 50 K) activation barriers postulated by Pineau des Forets et al. (1990) for the neutral-neutral reactions (see §3) involved in the nitrogen chemistry.

³We set the Doppler parameter equal to 2 km s^{-1} for all absorption lines. As in SD95, we include H₂ transitions in the Lyman and Werner bands, neglecting the rotational structure. We use the Federman et al. (1979) self-shielding formulae for H₂, and the van Dishoeck & Black (1989) shielding function for CO.

where ω is the grain albedo and p_i are the photoabsorption “efficiency factors” (Gredel et al. 1989). We adopt the efficiency factors p_i listed in the UMIST99 compilation, and we set $\omega = 0.5$ (SD95).

Molecule formation requires the presence of H_2 . We assume that hydrogen molecules are formed on grain surfaces with a rate coefficient

$$R = 3 \times 10^{-18} T^{1/2} y_F \text{ cm}^3 \text{ s}^{-1} \quad (4)$$

where T is the gas temperature, and y_F is a “formation efficiency” that depends primarily on the grain temperature (Manic et al. 2001; Biham et al. 2001, 2002; Cazaux & Tielens 2002; Vidali et al. 2004). We set $y_F = 1$ appropriate for low-temperature ($\sim 10 - 20$ K) dust grains. We do not consider accretion or ejection of other molecular species onto, or from, the grains.

PDRs consist of several distinct zones or layers with sizes and locations that depend on the gas density and FUV field strength. As discussed by SD95, these include the outer H I zone, followed by the C II, S II, and Si II zones, terminated by a fully cosmic-ray dominated dark core. In the H I zone, rapid photodissociation keeps the hydrogen in atomic form. In the C II zone, the hydrogen “self-shields” and becomes molecular, but photoionization maintains the carbon as C^+ . In the S II, zone the carbon is fully incorporated into CO, but photoionization and charge-transfer maintain the sulfur as S^+ . In the Si II layer the silicon is maintained as Si^+ , but the sulfur is either atomic or is incorporated into molecules. The relative efficiencies of the various molecular formation sequences, and the resulting molecular densities, vary with cloud depth and from zone to zone. For example, in the model considered by SD95, for which the hydrogen particle density $n = 10^6 \text{ cm}^{-3}$ and $\chi = 2 \times 10^5$, the CN/HCN density ratio is large (~ 10) in the the H I, C II, and S II layers, but then decreases and becomes small ($\sim 10^{-4}$) in the dark core. A large CN/HCN ratio was therefore identified as an important feature of (dense) PDRs. SD95 identified additional molecular diagnostic ratios of FUV irradiated gas, including $\text{OH}/\text{H}_2\text{O}$, CO^+/HCO^+ , and SO^+/SO (see also Sternberg et al. 1996).

The sizes and locations of the various zones also depend on the total gas-phase elemental abundances. In our calculations we set the gas-phase elemental abundances equal to the interstellar values observed in the diffuse cloud toward $\zeta \text{ Oph}$. Thus, we set $\text{C}/\text{H} = 1.32 \times 10^{-4}$ (Cardelli et al. 1993), $\text{N}/\text{H} = 7.50 \times 10^{-5}$ (Meyer et al. 1997), $\text{O}/\text{H} = 2.84 \times 10^{-4}$ (Meyer et al. 1998), $\text{Si}/\text{H} = 1.78 \times 10^{-6}$ (Cardelli et al. 1994), and $\text{S}/\text{H} = 8.30 \times 10^{-6}$ (Lepp et al. 1988). We adopt a helium abundance $\text{He}/\text{H} = 0.1$. In most of our models we keep the gas-phase abundances fixed at these values, and independent of cloud depth. In one model we examine the effect of reducing the S (and Si) abundances by a factor of 100.

In this paper, we study the behavior in cool isothermal clouds. Our results are insensitive to the temperature for $T \lesssim 200$ K, and we adopt a representative gas temperature of $T = 50$ K. We consider isobaric clouds, so that the total hydrogen particle densities $n \equiv n_{\text{H}} + n_{\text{H}_2}$ are constant through the clouds. The densities of all other species increase by a factor of 2 at the H to H₂ transition layer. We present results for n ranging from 10^2 to 10^6 cm⁻³.

Explicit thermal balance computations (Sternberg & Dalgarno 1989; Burton et al. 1990) show that in dense ($n \gtrsim 10^4$ cm⁻³) PDRs the temperatures in the outer H I zones may exceed 10^3 K. Molecular synthesis may then proceed via a “hot gas” chemistry in a thin outer layer (e.g. via the efficient production of the reactive intermediate OH). However, the contributions to the total CN and HCN column densities from the hot layers are expected to be small (SD95). Here we exclude considerations of hot gas, and focus on the chemistry in the more extended cooler regions.

3. CN and HCN Formation and Destruction

There are three major pathways to the gas-phase formation of CN and HCN, as illustrated in Figures 2-4. In pathway #1, production occurs via the formation of carbon hydrides and intermediate CH and CH₂ radicals. In pathway #2 an additional route to CN (but not HCN) occurs via oxygen hydrides and the intermediates OH and NO. In pathway #3 the molecules are produced via nitrogen hydrides and parent H₂CN⁺ ions. We describe each of these pathways in turn.

3.1. Pathway #1

In pathway #1, which is important at all cloud depths, CN and HCN are formed via the neutral-neutral reactions ⁴



and



⁴Reactions (R1) and (R2) play central roles in the formation of CN and HCN. In our computations we assume a rate coefficient of 2.0×10^{-10} cm³ s⁻¹ at 50 K for (R1), as implied by pulsed laser experiments in room-temperature discharge flows, and a theoretical extrapolation to low temperature (Brownsword et al. 1996). This is an order-of-magnitude larger than the rate coefficient reported by Messing et al. (1981), and widely used in many previous PDR models including SD95. For Reaction (R2) we use the theoretical value of 5.9×10^{-11} cm³ s⁻¹ recently calculated by Herbst et al. (2000).

The required CH and CH₂ intermediates are produced in three ways. First is via radiative association



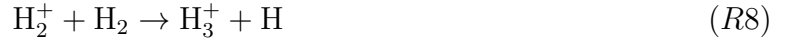
followed by rapid abstraction



and dissociative recombination



Second is cosmic-ray driven proton transfer



followed by



and then (R4), (R5), and (R6).

A third possibility is direct formation ⁵ via slow radiative association



which may become competitive in dense clouds where the fractional ionizations and the relative H₃⁺ densities, $n_{\text{H}_3^+}/n$, become small.

In the outer PDR, the CH and CH₂ radicals are removed by FUV photodissociation and photoionization. In shielded regions they are removed by



in rapid reactions with the available oxygen atoms.

⁵Reaction (R11) was not included in the SD95 study. Here we adopt $k_{11} = 1.0 \times 10^{-17} \text{ cm}^3 \text{ s}^{-1}$ for the rate coefficient (Smith et al. 2004).

3.2. Pathway #2

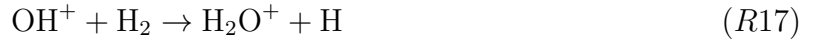
Pathway #2 is an additional route to CN (but not HCN), and becomes important mainly in shielded regions. In this pathway CN is formed via the intermediates OH and NO in the reaction pair



The main source of OH is cosmic-ray driven proton transfer



followed by abstractions



and dissociative recombination



Major removal mechanisms for OH and NO are photodissociation, and reactions with atomic oxygen and nitrogen



in the shielded regions.

3.3. Pathway #3

Finally, in pathway #3 both CN and HCN are produced via dissociative recombination



where the parent H_2CN^+ ions are formed via



followed by



This pathway is mainly important in shielded regions, but may also operate in the outer H I zone.

In shielded regions, where the N_2 density becomes large, NH and NH_2 are produced by the cosmic-ray driven sequence



followed by



In the H I zone, NH may be formed via



where H_2^* refers to the sum over all FUV-pumped hydrogen molecules in vibrational states with energies large enough to overcome the endothermicity of the reaction.

3.4. Destruction

The CN and HCN density profiles also depend on the varying efficiencies of the destruction mechanisms. In the outer PDR, photodissociation



dominates. In shielded layers the CN radical is removed by



Reaction (R38) dominates at intermediate cloud depths where a high abundance of nitrogen atoms are maintained by photodissociation. At large depths (R39) becomes the dominant removal process. The saturated HCN molecule is removed primarily by cosmic-ray induced photodissociation



Photodissociation of HCN operates as an important source of CN, both in the PDR and in the dark core. Additional removal processes for HCN in the dark core are



Reaction (R41) is important in low density clouds ($n \lesssim 10^3 \text{ cm}^{-3}$) where a large proton density is maintained by cosmic-ray ionization. Reaction (R42) becomes important in dense clouds ($n \gtrsim 10^3 \text{ cm}^{-3}$).

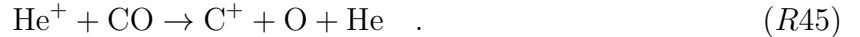
3.5. Free Carbon: C^+ and C

The efficiencies of the CN and HCN formation sequences depend on the availability of “free carbon” particles, either as C^+ ions or C atoms. As we discuss in §4, the CN and HCN profiles are closely related to the C^+ and C density distributions.

In the outer parts of the PDR, C^+ is produced by FUV photoionization



In shielded regions the main source is cosmic-ray driven helium-impact dissociative ionization of CO



In the outer PDR, where the electron density is high, the C^+ ions are removed by radiative recombination

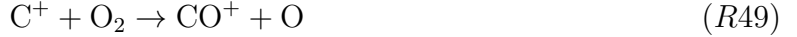


In shielded regions, radiative association (R3), and charge transfer neutralization



become important. Charge transfer with atomic sulfur plays a particularly important role in the partially shielded layers. In the dark core





dominate.

Carbon atoms are produced by radiative recombination and charge transfer ([R46] and [R47]), FUV photodissociation



and cosmic-ray induced photodissociation



The C atoms are removed by photoionization in the outer PDR, by proton transfer and radiative association ([R9] and [R11]), and cosmic-ray induced photoionization



at intermediate depths, and by



in the shielded cores.

4. Reference Model

The results of our model calculations are displayed in Figures 5, 6, and 7, which show cuts through the χ , n , ζ parameter space we have considered. For each set of cloud parameters we display the C^+ , C, CO, CN, and HCN densities (cm^{-3}) and column densities (cm^{-2}), as well as the CN/HCN density and column density ratios, as functions of A_V . The column densities are integrated from the cloud surface, in the normal direction. We also display the electron density profiles.

We first discuss our results for a specific “reference model”, with $n = 10^4 \text{ cm}^{-3}$, $\chi = 2 \times 10^3$, and $\zeta = 5 \times 10^{-17} \text{ s}^{-1}$. We use this model to analyze the depth dependent formation sequences and resulting density profiles. We also use it as a point of comparison as the cloud parameters are varied. Our reference model is displayed in panels (c), (d), and (e) of Figure 5, and again in Figures 6 and 7.

In our reference model, and in our parameter study we adopt $T = 50 \text{ K}$. For our assumed set of reaction rate coefficients, the results we describe below are quite insensitive

to the assumed gas temperature, provided the gas is cold with $T \lesssim 200$ K. For example, relative to our results for 50 K, the CN and HCN densities change by less than a factor of 2 at all A_V , if T is decreased to 20 K, or increased to 200 K.

4.1. C⁺, C, and CO Density Profiles

The C⁺, C, and CO density profiles in our reference model show the familiar structure seen in numerous PDR calculations (Tielens & Hollenbach 1985; van Dishoeck & Black 1988; Le Bourlot et al. 1993a; Flower et al. 1994; SD95; Jansen et al. 1995; Bakes & Tielens 1998). The carbon is ionized in the outer layers, and undergoes a conversion to CO as the ionizing FUV radiation is attenuated. An important feature is the double peaked atomic carbon density profile.

The first C peak is associated with the sharp transition of the available gas-phase carbon from fully ionized to molecular form near the inner edge of the C II zone. In our reference model this occurs at $A_V = 2$. Due to the rapid production of CO at this location, the C density at the peak reaches only $\sim 20\%$ of the total gas-phase carbon abundance. The transition is, effectively, directly from C⁺ to CO. After the conversion to CO only trace quantities of C and C⁺ remain.

An important property of the C⁺/C/CO transition region is that photodissociation of CO continues to dominate the production of the free carbon well beyond the point where the conversion to CO is complete. For example, in our reference model, photodissociation dominates up to $A_V = 2.5$, well inside the S II zone. Up to this point, C⁺ continues to be produced by photoionization, and the C⁺/C density ratio is set by the balance between recombination and photoionization. Thus, in the C II zone, where the production rate of atomic carbon via recombination is constant (since $n_e \approx n_{C^+}$), the C density increases as the photoionization rate is attenuated. However, once the conversion to CO is complete the atomic carbon density drops as the CO photodissociation rate decreases. This behavior gives rise to the first C peak.

We note that for PAH abundances $\gtrsim 10^{-7}$ mutual neutralization, $C^+ + PAH^- \rightarrow C + PAH$, can compete with radiative recombination (Lepp et al. 1988) leading to a slight shift in the positions of the C⁺/C/CO transition layers (Bakes & Tielens 1998). We do not include the effects of PAHs in our analysis. Similarly, the process of “grain-assisted” ion-electron recombination may become important when $n_e \alpha_r / n \alpha_g < 1$, where α_r (equal to $1.4 \times 10^{-11} \text{ cm}^{-3} \text{ s}^{-1}$ at 50 K, for C⁺ ions), and $\alpha_g \lesssim 10^{-14} \text{ cm}^3 \text{ s}^{-1}$ are the radiative and grain-assisted recombination rate coefficients. The efficiency of grain-assisted recombination

depends on the grain population size distribution and on the grain charge (Weingartner & Draine 2001). In the computations we present here we exclude this process. Including it can increase the C densities at the first C peak. We have verified that the CN and HCN density profiles we discuss below are not affected significantly.

At larger depths, e.g. for $A_V > 2.5$ in our model, the rate of CO photodissociation becomes vanishingly small, and the primary source of free carbon becomes cosmic-ray driven helium-impact ionization of CO ([R44] and [R45]). The resulting C^+ ions are neutralized by radiative recombination (R46), and by rapid charge transfer of the C^+ ions with S atoms (R47). The rapid neutralization keeps the free carbon in atomic form, so that $n_C/n_{C^+} \gg 1$. Because the rate of helium impact ionization is independent of cloud depth, the C density *increases* with A_V so long as photoionization dominates the removal of the carbon atoms, and as the photoionization rate is attenuated. The second C peak occurs at the point where radiative association with H_2 (R11), cosmic-ray induced photoionization (R52), and proton transfer reactions with H_3^+ (R9) begin to dominate the removal of the carbon atoms. In our reference model this occurs at $A_V = 3.7$.

The C density at this location may be estimated analytically,

$$n_C \approx \frac{\zeta X_{\text{He}}}{2p_{52}\zeta/n + k_9 n_{H_3^+}/n + k_{11}} \quad (5)$$

where $k_9 = 2.0 \times 10^9$ and $k_{11} = 1.0 \times 10^{-17} \text{ cm}^3 \text{ s}^{-1}$ are the rate coefficients for (R9) and (R11), the parameter $p_{52} = 1.0 \times 10^3$ is the efficiency factor for (R52), and $X_{\text{He}} = 0.1$ is the He abundance. The first two terms in the denominator becomes small for $n \gtrsim 10^4 \text{ cm}^{-3}$, and n_C is then independent of n . In this limit, $n_C \approx 0.25 \text{ cm}^{-3}$ for $\zeta = 5 \times 10^{-17} \text{ s}^{-1}$, in good agreement with the numerical value of 0.40 cm^{-3} at the second C peak. Beyond this point the C density decreases, particularly as the O_2 and SO densities rise and as the removal reactions (R53), (R54) and (R55) become more effective. A sharp drop in the C density occurs at $A_V \approx 7$, and the C density finally stabilizes to a value of $3.6 \times 10^{-4} \text{ cm}^{-3}$ in the cosmic-ray dominated dark core. The atomic carbon density in the core depends on n and ζ as discussed further in §5.

The second C peak marks the point where removal of the C atoms by FUV photoionization becomes inefficient compared to chemical reactions and cosmic-ray induced photoionization. The minimum between the two atomic carbon peaks occurs near to the point where helium impact dissociative ionization of CO replaces photodissociation of CO as the primary source of free carbon particles.

4.2. CN and HCN Profiles

In our reference model a pronounced peak is present in the CN density profile at $A_V = 2$, at the inner edge of the C II zone, and close to the location of the first C peak. A small HCN peak is also present at this location. Throughout the C II zone, the CN and HCN molecules are produced primarily via pathway #1, where the formation of the CH and CH₂ intermediates is initiated by radiative association of C⁺ with H₂ (R3). The CN density peak occurs where the C⁺ density is still close to its maximum possible value, but where the photodissociation rates are diminished. The CN density then decreases with cloud depth as the C⁺ density drops across the C⁺/C/CO transition layer.

Because the carbon is fully ionized in the C II zone, molecule formation is “recombination limited” in this part of the cloud. The CN density at the inner edge of the C II zone may therefore be expected to scale linearly with the gas density n for a fixed value of the “ionization parameter” χ/n . This may be seen analytically by writing

$$n_{\text{CH}} \approx \frac{k_3 n_{\text{C}^+} n_{\text{H}_2}}{\chi \Gamma'_{\text{CH}}} f_{\text{CH}} \approx \frac{k_3}{\chi \Gamma'_{\text{CH}}} f_{\text{CH}} X_{\text{C}} n^2 \quad (6)$$

and

$$n_{\text{CN}} \approx \frac{k_1 n_{\text{CH}} n_{\text{N}}}{\chi \Gamma'_{\text{CN}}} \approx \frac{k_1 k_3}{\Gamma'_{\text{CH}} \Gamma'_{\text{CN}}} f_{\text{CH}} X_{\text{C}} X_{\text{N}} \left(\frac{n}{\chi}\right)^2 n \quad (7)$$

In these expressions, $k_1 = 2.0 \times 10^{-10}$ and $k_3 = 5.7 \times 10^{-16} \text{ cm}^3 \text{ s}^{-1}$ are the rate coefficients for reactions (R1) and (R3), and $\chi \Gamma'_{\text{CH}} = 1.7 \times 10^{-8}$ and $\chi \Gamma'_{\text{CN}} = 5.0 \times 10^{-10} \text{ s}^{-1}$ are the *attenuated* photodissociation rates at the inner edge of the C II zone. The fraction of recombining of CH₃⁺ ions that fragment to CH is $f_{\text{CH}} = 0.43$, and $X_{\text{C}} = 1.32 \times 10^{-4}$ and $X_{\text{N}} = 7.50 \times 10^{-5}$ are the gas phase abundances of carbon and nitrogen. For $n = 10^4 \text{ cm}^{-3}$ and $\chi = 10^3$ this gives $n_{\text{CN}} = 5.7 \times 10^{-5} \text{ cm}^{-3}$, in good agreement with our numerically computed value of $9.0 \times 10^{-5} \text{ cm}^{-3}$ at the peak. The photo-attenuation factors (see equation [2]) depend on the visual extinctions at the termination points of the C II zones, and therefore scale with χ/n . Equation (7) shows that for fixed χ/n the CN density at the peak is proportional to the product of the carbon and nitrogen abundances and to the cloud density n , and is independent of χ . These simple scalings are verified by our numerical results in §5.

The CN density decreases as the supply of free carbon produced by CO photodissociation diminishes. However, when the primary source of free carbon switches to helium impact ionization, the CN density stops decreasing and a pronounced “plateau” appears in the density profile. In our reference model the CN density plateau extends from $A_V = 3$ to 6.

The CN density profile flattens for a combination of reasons. First, while the CH and CH₂ formation efficiencies decrease as the C⁺ disappears, this is offset by a more rapid decline

in the the CH and CH₂ photodestruction rates. Second, the *rise* in the atomic carbon density up to the second C peak leads to an increased efficiency of the proton-transfer sequence initiated by (R9) in pathway #1. Third, CN formation via pathway #2 also begins to play a significant role as the OH and NO densities increase.

Furthermore, while HCN (formed via [R2]) is removed by photodissociation, at these cloud depths CN is removed by neutral-neutral reactions with N atoms (R38). Photodestruction of CN is ineffective in the plateau because of the severe attenuation of the CN photodissociation rate (see Figure 1). Importantly, photodissociation of HCN becomes a major source of CN in the plateau. The HCN density therefore rises as the FUV field is attenuated, but because the atomic nitrogen density remains large throughout, the resulting CN density remains insensitive to A_V .

At these cloud depths molecule formation is “ionization limited” since only a trace amount of free-carbon is released from the CO molecules by helium impact ionization. Because CN is removed in reactions with a neutral species (N atoms), the CN density is proportional to the cosmic-ray ionization rate and independent of the gas density. For a simple analytic estimate we assume that CN formation is initiated by proton transfer in reactions of C with H₃⁺ (R9), or by radiative association of C with H₂ (R11), in pathway #1. We also assume and that every HCN formation event leads to CN via photodissociation. We assume further that the CH and CH₂ intermediates are removed by reactions with atomic oxygen [(R12) and (R13)], and that these reactions proceed with equal approximate rate coefficients $k_O = 2 \times 10^{-10} \text{ cm}^3 \text{ s}^{-1}$. Setting $k_N = 1 \times 10^{-10} \text{ cm}^3 \text{ s}^{-1}$ for both (R1) and (R2) it follows ⁶ that

$$n_{\text{CN}} \approx 0.5\zeta \frac{1}{k_{38}} \frac{k_N}{k_O} \frac{X_{\text{He}}}{X_{\text{O}}} \quad (8)$$

where $k_{38} = 3 \times 10^{-10} \text{ cm}^3 \text{ s}^{-1}$ is the rate coefficient for removal reactions of CN with N. Evaluating for $X_{\text{He}} = 0.1$, $X_{\text{O}} = 2.84 \times 10^{-4}$, and $\zeta = 5 \times 10^{-17} \text{ s}^{-1}$ yields $n_{\text{CN}} = 9 \times 10^{-6} \text{ cm}^{-3}$, in good agreement with the numerically computed $n_{\text{CN}} \approx 2 \times 10^{-5} \text{ cm}^{-3}$ in the CN plateau (see Figure 5). Thus, n_{CN} is proportional to ζ and independent of n , and with the above assumptions ⁷, is independent of both the gas-phase nitrogen and carbon abundances.

The CN density plateau is maintained up to the point where photodissociation by the incident FUV photons is the dominant HCN removal mechanism, or up to $A_V = 6$ in our

⁶The factor of 0.5 in this expression enters because the cosmic ray ionization rate of He is half that of H₂.

⁷These assumptions break down if, for example, $X_C > X_O$ so that C atoms become abundant rather than being mainly locked in CO, or if X_C becomes so small such that formation via pathway #1 becomes negligible.

reference model. The HCN density reaches a peak value of $8.6 \times 10^{-4} \text{ cm}^{-3}$ at this point. At larger depths cosmic-ray induced photodissociation becomes the dominant HCN destruction mechanism, proceeding at a rate independent of A_V . CN is removed by reactions with oxygen atoms (R39). The CN and HCN formation efficiencies both decline as less C and C^+ is available, and the CN and HCN densities decrease to their dark core values of 1.2×10^{-6} and $2.6 \times 10^{-5} \text{ cm}^{-3}$ respectively.

Figure 5e shows that the CN column density rise sharply to $N_{\text{CN}} = 6 \times 10^{12} \text{ cm}^{-2}$ at the CN peak at $A_V = 2$, and that much of the CN column is built up at this location. The HCN column remains small at $A_V = 2$, but continues to increase with cloud depth. N_{HCN} approaches $7 \times 10^{14} \text{ cm}^{-2}$ at $A_V = 6$ where the HCN volume density is at its maximum. The ratio $N_{\text{CN}}/N_{\text{HCN}} \sim 10$ at $A_V = 2$, and decreases to ~ 0.1 at $A_V = 6$ (see Figure 5f).

5. Parameter Study

5.1. Density

Figure 5 displays our results for n equal to 10^3 , 10^5 , and 10^6 cm^{-3} , in addition to our 10^4 cm^{-3} reference model, and illustrates the effects of varying the cloud density. In this sequence we keep the ionization parameter χ/n constant at 0.2 cm^{-3} , so that the $\text{C}^+/\text{C}/\text{CO}$ transition layers occur at the same location ($A_V = 2$) in all four models.

For fixed χ/n , the depth at which helium impact ionization of CO replaces photodissociation of CO as the source of free carbon, increases with the cloud density n . However, the depth at which removal of atomic carbon by photoionization becomes ineffective compared to proton transfer or radiative association ([R9] or [R11]), is independent of n . Therefore, the relative height of the second C peak (at $A_V = 4.2$) decreases with n , and the peak disappears at sufficiently high densities ($\gtrsim 10^5 \text{ cm}^{-3}$). For densities above 10^4 cm^{-3} , $n_{\text{C}} \approx 0.4 \text{ cm}^{-3}$ at this location, consistent with Equation (5). At lower densities all of the available carbon is atomic at the location of the second C peak, and n_{C} is then limited by the carbon abundance X_{C} (see Figure 5a).

At low n , the free carbon density remains relatively high at large A_V and in the dark core. At high n the free carbon density becomes small. As we discuss below, this behavior reflects the transition from the “high-ionization phase” to “low-ionization phase” in the cosmic-ray dominated core (Le Bourlot et al. 1993b; 1995; Lee et al. 2000). The asymptotic values of the C densities in the dark core influence the shapes of the atomic carbon density profiles at intermediate depths in the PDRs.

Figure 5 shows that the CN density at $A_V = 2$ increases linearly with n , from $\sim 10^{-5}$ to 10^{-2} cm^{-3} , in accordance with Equation (6). The “CN peak” becomes more pronounced as n increases. In the $n = 10^6$ cm^{-3} model, the density of FUV-pumped H_2 becomes large, and CN is also formed via pathway #3 initiated by (R35). For $n \geq 10^4$ cm^{-3} the “CN plateau” from $A_V = 3$ to ~ 6 is apparent. At these depths $n_{\text{CN}} \approx 2 \times 10^{-5}$ cm^{-3} independent of n , consistent with Equation (8). At low n , the CN density remains large to high A_V due to the elevated free carbon densities.

For fixed χ/n , FUV photodissociation of HCN is effective to greater depths as n increases. The location of the HCN density peak therefore moves from a visual extinction of 5.6 to 7.2 as the gas density is increased from 10^4 to 10^6 cm^{-3} . The column density ratio $N_{\text{CN}}/N_{\text{HCN}}$ remains large to greater depths as n is increased, but the density ratio $n_{\text{CN}}/n_{\text{HCN}}$ falls off sharply with A_V (see Figure 5).

5.2. FUV Intensity, Sulfur Abundance, and Cosmic-Ray Ionization Rate

In Figure 6, we set n equal to 10^4 cm^{-3} , and we vary χ from 2×10^2 to 2×10^6 . This illustrates the effects of varying the incident FUV field intensity. The location of the $\text{C}^+/\text{C}/\text{CO}$ transition layer moves from $A_V = 1.3$ to 3.5 for this density and range of FUV intensities. The position of the second C peak is also shifted to larger A_V , as is the location of the sharp drop in the C density, which moves from $A_V = 6$ to 9. The approach to the dark-core conditions occurs at greater A_V as χ is increased.

Correspondingly, the locations of the CN peak and the inner HCN peak also move inward as χ is increased. Because the CN photodissociation rate declines most rapidly with A_V (see Figure 1) $n_{\text{CN}}/n_{\text{HCN}}$ and $N_{\text{CN}}/N_{\text{HCN}}$ at the CN peak increase with χ , from ~ 10 to 40 in our models.

In Figure 7, we show the effects of a reduced gas-phase S (and Si) abundance, and an increased cosmic-ray ionization rate, for our $n = 10^4$ cm^{-3} and $\chi = 10^3$ model. In panels (a), (b), and (c) of Figure 7, the S (and Si) abundances are reduced by a factor of 100. Charge transfer (R47) between C^+ and S is then less effective as a neutralizing mechanism, and the second C peak at large A_V is reduced. The formation efficiency of HCN in pathway #1, via radiative association of C with H_2 (R11) followed by the reaction of CH_2 with N (R2), is therefore also diminished, leading to a reduction of the inner HCN density peak (compare Fig. 7a and Fig. 7d). The resulting CN/HCN ratios are therefore enhanced in the CN plateau region, and in the dark core.

The bottom two rows of Figure 7 show the effects of increasing the cosmic-ray ionization

rate, by factors of 3 and 10, to 1.5×10^{-16} and $5 \times 10^{-16} \text{ s}^{-1}$. Increasing ζ mainly affects the atomic carbon density profile. The first C peak is unaltered because it is controlled by purely photo-processes. However, the second C peak is enhanced by the increased rate of helium impact destruction of CO (R44). The behavior is consistent with Equation (5). Initially, the C density increases linearly with ζ . However, for sufficiently large ζ the atomic carbon is removed by cosmic-ray induced photoionization (R52) and proton transfer reactions with H_3^+ (R9), rather than by radiative association with H_2 (R11). In this limit the C density is independent of ζ , and all of the available gas phase carbon becomes atomic, as occurs for our $\zeta = 5 \times 10^{-16}$ model.

The free carbon densities remain large throughout the cloud for high ζ . As we now discuss, the shift from a low to high free carbon density with increasing ζ is related to a “phase change” that occurs in the dark core.

5.3. Dark Core

In Figure 8 we display the densities, n_i , and density fractions, n_i/n , for C^+ , C, CO, CN, HCN, and free electrons, for fully opaque dark core conditions. Externally incident FUV photons are excluded, and the chemistry is driven entirely by cosmic-ray ionization. For these conditions, it follows from Equation (1) that the density fractions n_i/n depend on a single parameter, the ratio of the cloud density to the ionization rate. In Figure 8 we plot the solutions as functions of n/ζ_{-17} , where ζ_{-17} is the cosmic-ray ionization rate normalized to $1.0 \times 10^{-17} \text{ s}^{-1}$. The phenomenon of “bistability” (Le Bourlot et al. 1993b, 1995; Lee et al. 2000) is apparent in Figure 8, where for densities between 370 and 675 cm^{-3} two stable solutions exist. A high-ionization phase (HIP) occurs at low n , and a low-ionization phase (LIP) occurs at high n . The two phases may coexist where the gas is bistable. We will present our own discussion of bistability elsewhere (Boger & Sternberg 2005). Because bistability occurs for a narrow range of densities the transition from the HIP to LIP may be said to occur near a “critical density” $n_{\text{crit}}/\zeta_{-17} \approx 500 \text{ cm}^{-3}$ (for our assumed gas-phase abundances). In our computations, $n_e/n \gtrsim 10^{-5}$ in the HIP, and $n_e/n \lesssim 10^{-6}$ in the LIP, and the fractional ionization drops by a factor ~ 10 , at the transition density. The C^+ and C densities are large in the HIP, with $n_{\text{C}}/n_{\text{CO}} \sim 1$, and small in the LIP, with $n_{\text{C}}/n_{\text{CO}} < 10^{-3}$, consistent with the findings of Flower et al. (1994). Correspondingly, n_{CN}/n and n_{HCN}/n are large for $n < n_{\text{crit}}$, and small for $n > n_{\text{crit}}$. Furthermore, $n_{\text{CN}}/n_{\text{HCN}}$ is large in the low-density HIP, and becomes small in the high-density LIP. In the HIP, $n_{\text{CN}}/n_{\text{HCN}}$ decreases from ~ 20 to 0.07 for n/ζ_{-17} ranging from 10 to 675 cm^{-3} . In the LIP, $n_{\text{CN}}/n_{\text{HCN}}$ decreases from 0.4 to 3×10^{-3} for n/ζ_{-17} ranging from 370 to 10⁵ cm^{-3} .

Returning now to Figure 7, we note that the increase in the free carbon density at large A_V that occurs as ζ is increased, is due to the rise in n_{crit} , and a corresponding transition from LIP to HIP conditions, for the specific gas density of 10^4 cm^{-3} . The phase transition is affected by the presence of some FUV radiation. For example, for $\zeta = 1.5 \times 10^{-16} \text{ s}^{-1}$ it occurs at $A_V \approx 7$ rather than in the fully opaque core (see Figure 7g). As the ionization rate is increased further, the gas is converted to the HIP throughout (see Figure 7j).

6. Discussion and Summary

CN and HCN molecules have been observed in a diversity of Galactic and extragalactic sources, and the CN/HCN intensity and density ratios have been used as diagnostic probes of FUV irradiated molecular gas. One recent and interesting example is the well-known starburst galaxy M82 ($d = 3.9 \text{ Mpc}$; $L = 3.7 \times 10^{10} L_{\odot}$; e.g. Förster-Schreiber et al. 2003). Fuente et al. (2005) have reported measurements of CN 1-0 (113.490 GHz), CN 2-1 (226.874 GHz), and HCN 1-0 (88.631 GHz) line emissions across the inner 650 pc star-forming molecular disk in M82. They find that $N_{\text{CN}}/N_{\text{HCN}} \sim 5$, and argue that the large ratio is indicative of a giant and dense PDR bathed in the intense field of the starburst. They derive $n \sim 10^4$ to 10^5 cm^{-3} , and $\chi \sim 10^4$. Fuente et al. (2005) conclude that $A_V \lesssim 5$ in the M82 clouds, since for optically thicker clouds the CN/HCN column density ratio would be smaller than observed. Our results provide support for these conclusions. In this picture ~ 10 to 20 individual clouds along the line of sight are required, since for characteristic elemental abundances the computed CN and HCN columns for $A_V \lesssim 5$ (see Figures 5 and 6) are about an order of magnitude smaller than observed ($N_{\text{CN}} = [2 \pm 0.5] \times 10^{14} \text{ cm}^{-2}$ and $N_{\text{HCN}} = [4 \pm 0.5] \times 10^{13} \text{ cm}^{-2}$).

Alternatively, the large CN/HCN ratio might be a signature of a very large cosmic-ray ionization rate, up to $\sim 5 \times 10^{-15} \text{ s}^{-1}$, as invoked by Suchkov et al. (1993) for M82 and other starburst galaxies. For such high ionization rates the CN/HCN ratio could remain $\gtrsim 1$ even in dense and opaque cores if these are maintained in the high-ionization phase. Our results indicate that for $\zeta = 5 \times 10^{-15} \text{ s}^{-1}$, the HIP is maintained up to $n \sim 4 \times 10^5 \text{ cm}^{-3}$ (see Figure 8). This possibility is perhaps more compatible with the large C/CO ratio $\gtrsim 0.5$ inferred from observations of the 492 and 809 GHz C I fine-structure lines in M82 (Schilke et al. 1993; Stutzki et al. 1997; see also Gerin & Phillips 2000). As discussed above, a large C/CO ratio is a signature of the HIP.

In this paper we have presented a theoretical study of CN and HCN molecule formation in dense interstellar clouds exposed to intense FUV radiation fields. We have analyzed the behavior of the CN/HCN density ratio for a wide range of conditions, with the aim of showing

how this molecular ratio may be used as a diagnostic probe of molecule formation in FUV irradiated gas. For this purpose, we have constructed detailed models in which we solve the equations of chemical equilibrium as functions of optical depth, for uniform density clouds at constant gas temperature (50 K). Our results are insensitive to the gas temperature for cold clouds with $T \lesssim 200$ K. We consider clouds with hydrogen particle densities ranging from $n = 10^2$ to 10^6 cm^{-3} , and FUV radiation intensities ranging from $\chi = 20$ to 2×10^5 , appropriate for star-forming clouds near young OB stars and clusters. We present results for cosmic-ray ionization rates ranging from 5×10^{-17} to 5×10^{-16} s^{-1} , and we also examine the effects of large (factor 100) sulfur depletions on the computed density profiles. We present calculations of the density profiles for CN and HCN, and for the associated species C^+ , C, and CO. We analyze the behavior from the outer FUV photon-dominated regions, into the fully opaque cosmic-ray dominated cores.

In this paper, we adopt a fixed characteristic shape for the FUV radiation spectrum, and we do not examine the possible signatures of “soft” versus “hard” FUV fields (van Zadelhoff et al. 2003). Time-dependent effects due to episodic shadowing (Störzer et al. 1997), fluctuating radiation fields (Parravano et al. 2003), grain processing (Charnley et al. 2001), turbulent mixing and diffusion (Papadopoulos et al. 2004), and other dynamical processes, are not considered here.

Our models show how observations of the CN/HCN abundances ratio in molecular clouds may be used as probes of FUV and cosmic-ray driven gas-phase chemistry for a wide range of conditions. We find that in dense gas, CN molecules are characteristically and preferentially produced near the inner edges of the C II zones in the PDRs. This is where C^+ begins to recombine and where atomic carbon is incorporated into CO. Molecule formation is “recombination limited” at these depths, and for fixed χ/n , the CN density is proportional to the cloud density, and to the gas-phase carbon and nitrogen abundances. For $n \gtrsim 10^4$ cm^{-3} , and for clouds with linear sizes corresponding to visual extinctions $A_V \lesssim 10$, the entire integrated CN column density is built up at the $\text{C}^+/\text{C}/\text{CO}$ transition layer. For characteristic interstellar carbon and nitrogen gas-phase abundances the predicted CN columns are $\sim 3 \times 10^{13}$ cm^{-2} . HCN is rapidly photodissociated in the outer parts of the PDRs including the $\text{C}^+/\text{C}/\text{CO}$ transition layers. Because HCN is more vulnerable to photodissociation, the CN/HCN density ratio is large at low A_V , and decreases with increasing optical depth. We find that the CN/HCN density ratio typically decreases from $\gtrsim 10$ in the $\text{C}^+/\text{C}/\text{CO}$ transition layers to $\lesssim 0.1$ in the opaque cores.

At intermediate and large depths, the bulk of the gas-phase carbon is locked in CO molecules, and the CN and HCN densities depend on the rate at which carbon is released from CO by cosmic-ray driven helium impact ionization. Molecule formation is then “ionization

limited” and occurs with an efficiency proportional to the cosmic-ray ionization rate. In dense clouds, an enhanced abundance of atomic carbon is maintained at intermediate depths, where charge transfer of C^+ with S is effective, and where photo-destruction reduces the efficiency with which the carbon atoms are removed in reactions with molecules. At these intermediate depths the CN density is insensitive to A_V . However, the HCN densities increase with A_V as the destructive FUV photons are absorbed.

The C^+ , C, CO, CN, and HCN densities in the opaque cores depend on whether the cores are in the “low-ionization” or “high-ionization” phases that are possible for such gas. We present computations for gas in both phases. The transition from the HIP to LIP occurs at a critical value $n/\zeta_{-17} = 10^3 \text{ cm}^{-3}$, consistent with previous findings. The CN/HCN density ratio can become large $\gtrsim 1$ in the LIP, but remains small in the HIP.

For dense gas in Galactic molecular clouds, and for characteristic cosmic-ray ionization rates, a large CN/HCN density ratio may be interpreted reliably as an indicator of molecule formation in PDRs. In clouds exposed to enhanced fluxes of cosmic-rays, as perhaps occurs in starburst galaxies, a high CN/HCN ratio may alternatively be an indicator of opaque clouds in the high-ionization phase. Measurements of the C/CO ratio can be used to distinguish between these two possibilities.

Acknowledgments

We thank A. Dalgarno, A. Fuente, O. Gnat, E. Herbst, and C.F. McKee for discussions, and the referee for helpful comments and suggestions. This research is supported by the Israel Science Foundation, grant 221/03.

REFERENCES

- Bachiller, R., Fuente, A., Bujarrabal, V., Colomer, F., Loup, C., Omont, A., & de Jong, T. 1997, *A&A*, 319, 235
- Bachiller, R., Forveille, T., Huggins, P.J., & Cox, P. 1997, *A&A*, 324, 1123
- Bakes, E.L.O., & Tielens, A.G.G.M. 1998, *ApJ*, 499, 258
- Biham, O., Furman, I., Pirronello, V., & Vidali, G. 2001, *ApJ*, 553, 595
- Biham, O., & Lipshtat, A. 2002, *Phys. Rev. E*, 66, 056103

- Boger, G., & Sternberg, A. 2005, in prep.
- Brittain, S.D., Simon, T., Craig, K., & Terrence, R.W. 2004, ApJ, 606, 911
- Brownsword, R.A., Gatenby, S.D., Herbert, L.B., Smith, I.W.M., Stewart, D.W.A., & Symonds, A.C. 1996, J. Chem. Soc. Faraday Trans., 92, 723
- Burton, M.G., Hollenbach, D.J., & Tielens, A.G.G.M. 1990, ApJ, 620, 639
- Cardelli, J.A., Mathis, J.S., Ebbets, D.C., & Savage, B.D. 1993, ApJ, 402, L17
- Cardelli, J.A., Sofia, U.J., Savage, B.D., Keenan, F.P., & Dufton, P.L. 1994, ApJ, 420, L29
- Cazaux, S., & Tielens, A.G.G.M. 2002, ApJ, 575, L29
- Charnley, S.B., Rodgers, S.D., & Ehrenfreund, P. 2001, A&A, 378, 1024
- de Boisanger, C., Helmich, F.P., & van Dishoeck, E.F. 1996, AA, 310, 315
- Draine, B.T. 1978, ApJS, 36, 595
- Draine, B.T. 2003, ARA&A, 41, 241
- Federman, S.R., Glassgold, A.E., & Kwan, J. 1979, ApJ, 227, 466
- Flower, D.R., Le Boulrot, J., Pineau Des Forets, G., & Roueff, E. 1994, \AA , 282, 225
- Förster-Schreiber, N.M., Genzel, R., Lutz, D., & Sternberg, A. 2003, ApJ, 599, 193
- Fuente, A., Martin-Pintado, J., Cernicharo, J., & Bachiller, R. 1993, A&A, 276, 473
- Fuente, A., Martin-Pintado, J., & Gaume, R. 1995, ApJ, 442, L33
- Fuente, A., & Martin-Pintado, J. 1997, ApJ, 477, L107
- Fuente, A., Rodriguez-Franco, A., Garcia-Burillo, S., Martin-Pintado, J., & Black, J.H. 2003, A&A, 406, 899
- Fuente, A., Garcia-Burillo, S., Gerin, M., Teyssier, D., Usero, A., Rizzom J.R., & de Vicente, P. 2005, ApJ, 619, L155
- Garcia-Burillo, S., Martin-Pintado, J., Fuente, A., Usero, A., & Neri, R. 2002, ApJ, 575, L55
- Gerin, M., & Phillips, T.G. 2000, ApJ, 537, 644

- Greaves, J.S., & Church, S.E. 1996 MNRAS, 283, 1179
- Gredel, R., Lepp, S., Dalgarno, A., & Herbst, E. 1989, ApJ, 347, 289
- Herbst, E., Lee, H.-H., Howe, D.A., & Millar, T.J. & 1994, MNRAS, 268, 335
- Herbst, E., Terzieva, R., & Talbi, D. 2000, 311, 869
- Hollenbach, D.J., & Tielens, A.G.G.M. 1997, ARA&A, 35, 179
- Jansen, D.J., van Dishoeck, E.F., Black, J.H., Spaans, M., & Sosin, C. 1995, A&A, 302, 223
- Jensen, M.J., Bilodeau, R.C., Safvan, C.P., Seiersen, K., Andersen, L.H., Pedersen, H.B., & Heber, O. 2000, ApJ, 543, 764
- Johnstone, D., Boonman, A.M.S., & van Dishoeck, E.F. 2003, A&A, 412, 157
- Knauth, D.C., Federman, S.R., Pan, K., Yan, M., & Lambert, D.L. 2001, ApJS, 135, 201
- Larson, A. et al. 1998, ApJ, 505, 459
- Le Bourlot, J., Pineau Des Forets, G., Roueff, E., & Flower, D.R. 1993, A&A, 267, 233
- Le Bourlot, J., Pineau des Forets, G., Roueff, E., & Schilke, P. 1993, ApJ, 416, L87
- Le Bourlot, J., Pineau des Forets, G., & Roueff, E. 1995, A&A, 297, 251
- Lee, H.-H., Bettens, R.P.A., & Herbst, E., & 1996, A&A, 119, 111
- Lee, H.-H., Roueff, E., Pineau des Forets, G., Shalabiea, O. M., Terzieva, R., & Herbst, Eric 1998, A&A, 334, 1047
- Lepp, S., Dalgarno, A., van Dishoeck, E.F., & Black, J.H. 1988, ApJ, 329, 418
- Le Teuff, Y.H., Millar, T.J., & Markwick, A.J 2000, A&A, 146, 157
- Lindqvist, M., Schier, F.L., Lucas, R., & Olofsson, H. 2000, A&A, 361, 1036
- Maloney, P.R., Hollenbach, D.J., & Tielens, A.G.G.M. 1996, ApJ, 466, 561
- Manic, G., Ragan, G., Pirronello, V., Roser, J.E., & Vidali, G. 2001, ApJ, 548, L253
- McCall, B.J. et al. 2003, Nature, 422, 500
- Meier, D.S., & Turner, J.L. 2005, ApJ, 618, 259
- Messing, I., Filseth, S.V., Sadowski, C.M., & Carrington, J. 1981, Chem.Phys., 74, 374

- Meyer, D.M., Cardelli, J.A., & Sofia, U.J. 1997, ApJ, 490, L103
- Meyer, D.M., Jura, M., & Cardelli, J.A. 1998, AJ, 493, 222
- Oppenheimer, M., & Dalgarno, A. 1974, ApJ, 192, 29
- Parravano, A. Hollenbach, D.J., & McKee, C.F. 2003, ApJ, 584, 797
- Papadopoulos, P.P., Thi, W.-F., & Viti, S. 2004, MNRAS, 351, 147
- Pineau des Forets, G., Roueff, E., & Flower, D.R. 1990, MNRAS, 244, 668
- Prasad, S.S., & Huntress, W.T., Jr. 1980, ApJS, 43, 1
- Roberge, W.G., Jones, D., Lepp, S., & Dalgarno, A. 1991, ApJS, 77, 287
- Savage, C., Apponi, A.J., Ziurys, L.M., & Wyckoff, S. 2002, ApJ, 578, 211
- Schilke, P., Walmsley, C. M., Pineau Des Forets, G., Roueff, E., Flower, D. R., & Guilloteau, S. 1992, *Å*, 256, 595
- Schilke, P., Carlstrom, J.E., Keene, J., & Phillips, T. G. 1993, ApJ, 417, L67
- Schneider, N., Simon, R., Kramer, C., Kraemer, K., Stutzki, J., & Mookerjea, B. 2003, A&A, 406, 915
- Simon, R., Stutzki, J., Sternberg, A., & Winnewisser, G. 1997, A&A, 327, L9
- Sofia, U.J., Lauroesch, J.T., Meyer, D.M., & Cartledge, S.I.B. 2004, ApJ, 605, 272
- Spaans, M., & Meijerink, R. 2005, Ap&SS, 295, 239
- Sternberg, A., & Dalgarno, A. 1989, ApJ, 338, 197
- Sternberg, A., & Dalgarno, A. 1995, ApJS, 99, 565
- Sternberg, A., Yan, M., & Dalgarno, A. 1996, in IAU Symp. 178, *Molecules in Astrophysics: Probes and Processes*, ed. E.F. van Dishoeck (Dordrecht: Kluwer), p. 141
- Sternberg, A. 2004, in *The Dense Interstellar Medium in Galaxies*, eds. Pfalzner, S. et al. (Berlin: Springer), p. 423
- Störzer, H., Stutzki, J., & Sternberg, A. 1996, A&A, 310, 592
- Stutzki, J. et al. 1997, ApJ, 477, L33

- Suchkov, A., Allen, R.J., & Heckman, T.M. 1993, ApJ, 542, 547
- Tielens A.G.G.M., & Hollenbach, D. 1985, ApJ, 291, 722
- Thi, W.-F., van Zadelhoff, G.-J., & van Dishoeck, E.F. 2004, A&A, 425, 955
- Truong-Bach, Nguyen-Q-Rieu, Omont, A., Olofsson, H., & Johansson, L.E.B. 1987, A&A, 176, 285
- Turner, B.E., Pirogov, L., & Minh, Y.C. 1997, ApJ, 483, 235
- van Dishoeck, E.F. 1987, in Rate Coefficients in Astrochemistry, ed. T.J. Millar & D.A. Williams (Dordrecht: Kluwer), p. 49
- van Dishoeck, E.F., & Black, J.H. 1988, ApJ, 340, 273
- van Dishoeck, E.F. 2004, ARA&A, 42, 119
- van Zadelhoff, G.-J., Aikawa, Y., Hogerheijde, M.R., & van Dishoeck, E.F. 2003, ApJ, 397, 789
- Vejby-Christensen, L., Andersen, L.H., Heber, O., Kella, D., Pedersen, H.B., Schmidt, H.T., & Zafman, D. 1997, ApJ, 483, 531
- Viala, Y.P. 1986, A&A, 64, 391
- Vikor, L. et al. 1999, A&A, 344, 1027
- Vidali, G., Roser, J.E., Manic, G., & Pirronello, V. 2004, JGR, 109, E7, E10907S14
- Watson, W.D. 1974, ApJ, 188, 35
- Weingartner, J.C., & Draine, B.T. 2001, ApJ563, 842
- Williams, J.P., Bergin, E.A., Caselli, P., Myers, P.C., & Plume, R. 1998, ApJ, 503, 689
- Wootten, A., Lichten, S.M., Sahai, R., & Wannier, P.G. 1982, ApJ, 257, 151
- Young Owl, R.C., Meixner, M.M., Wolfire, M. Tielens, A.G.G.M., & Tauber, J. 2000, ApJ, 540, 886

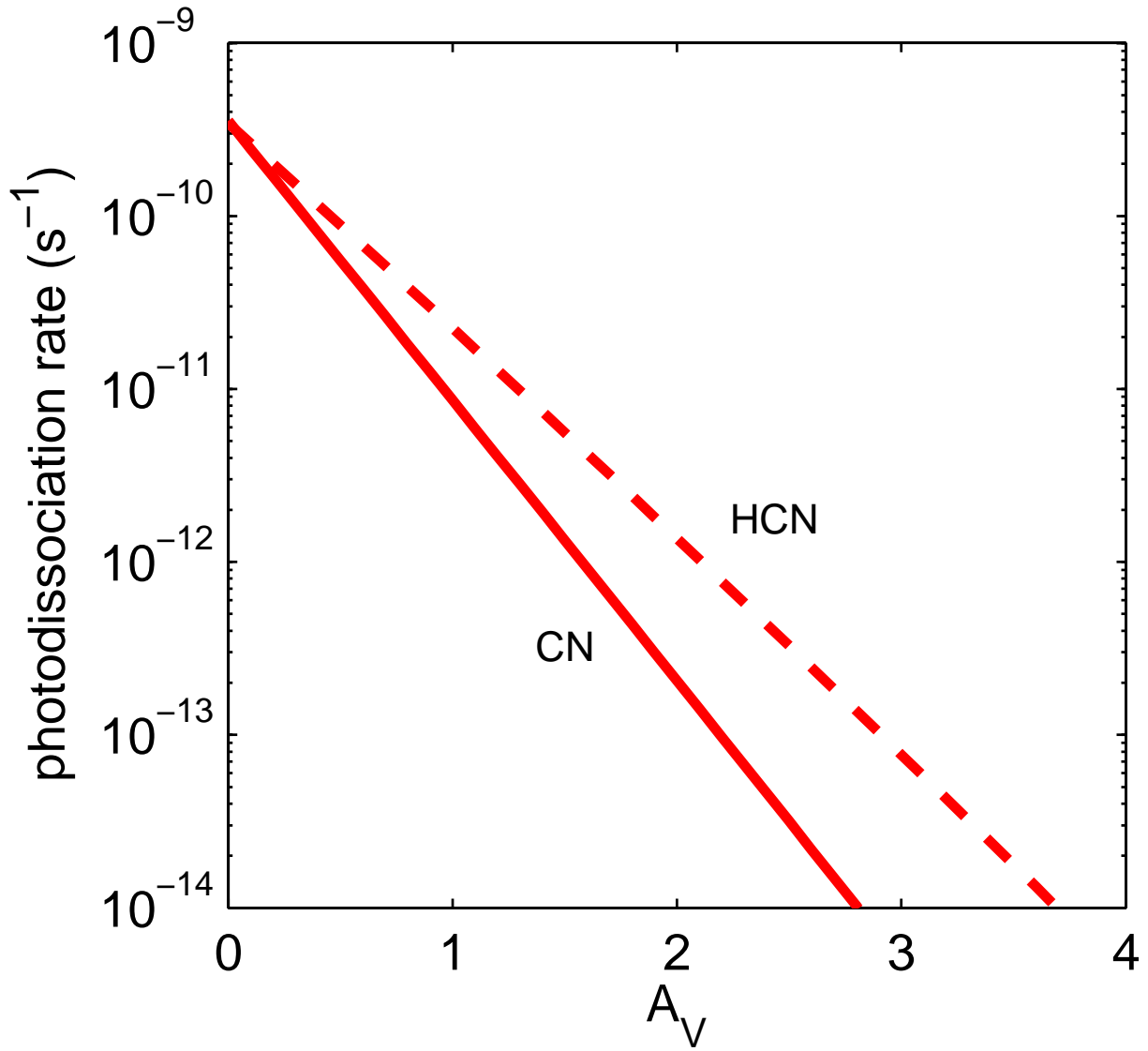


Fig. 1.— Photodissociation rates of CN and HCN as functions of visual extinction for a unit Draine field.

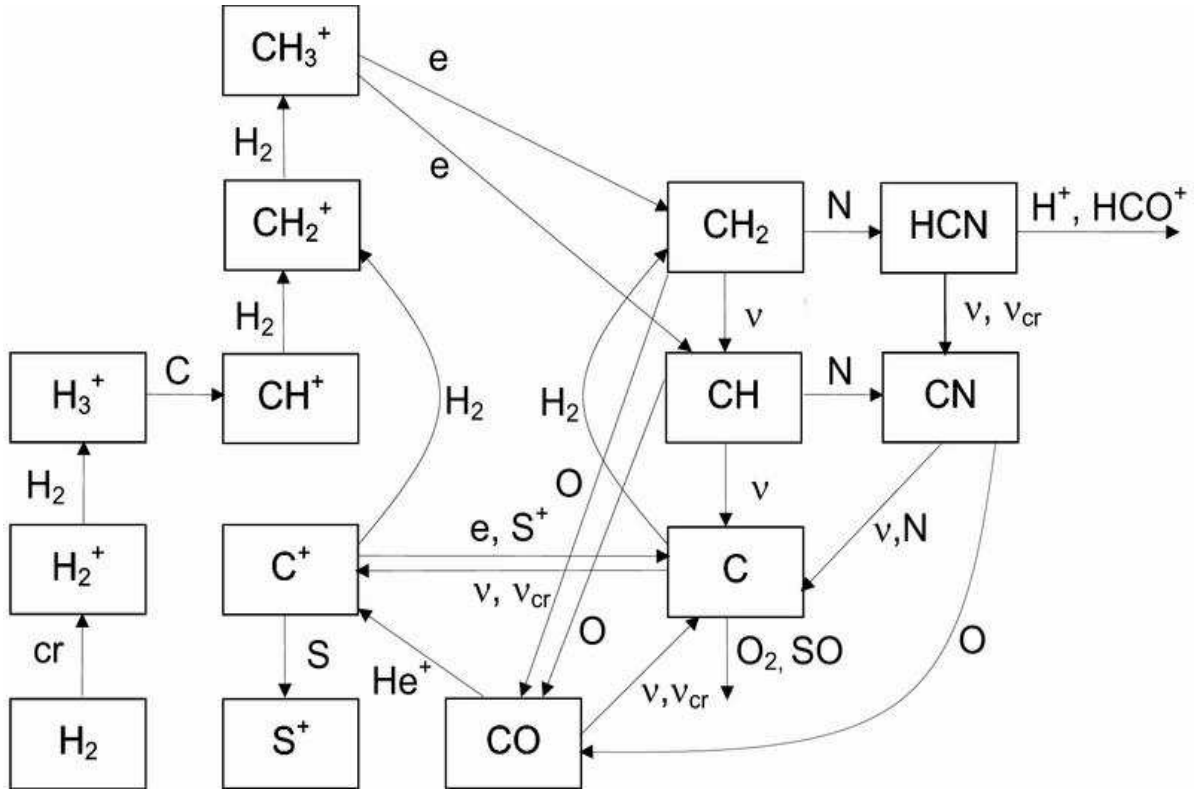


Fig. 2.— CN and HCN formation pathway #1 via carbon hydride intermediates.

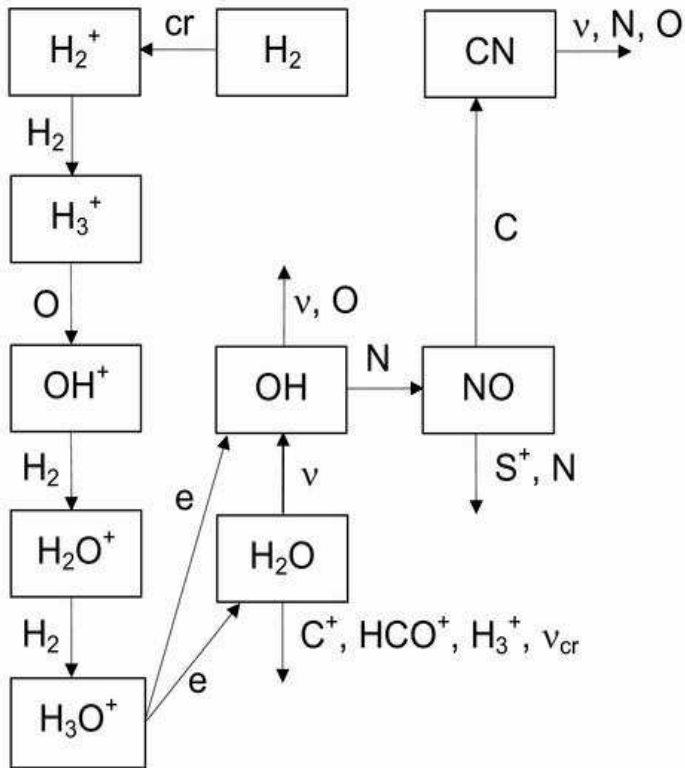


Fig. 3.— CN formation pathway #2 via oxygen hydride intermediates.

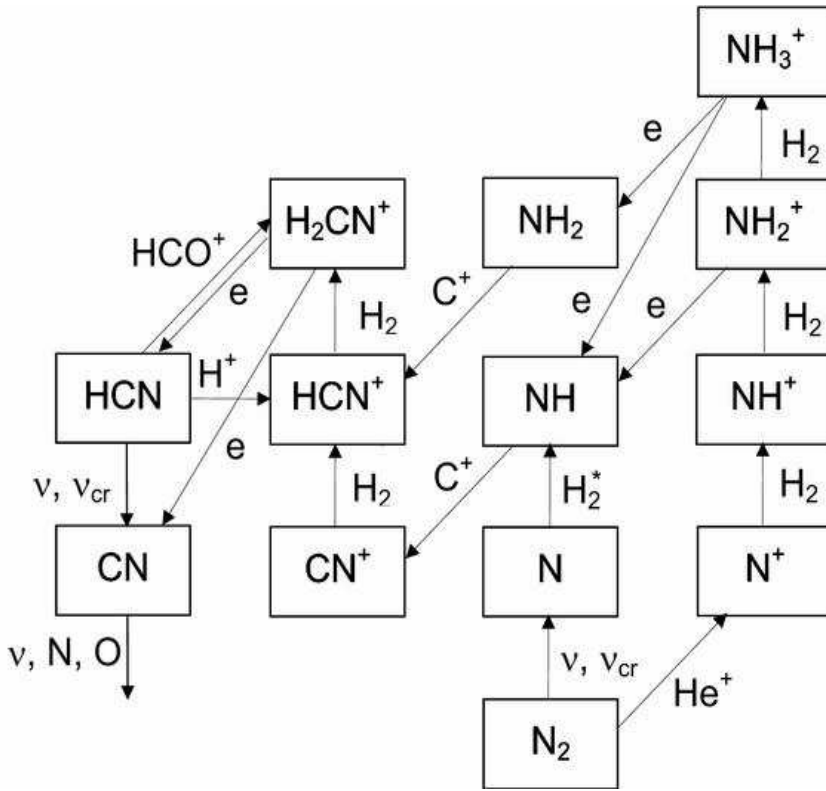


Fig. 4.— CN and HCN formation pathway #3 via nitrogen hydride intermediates.

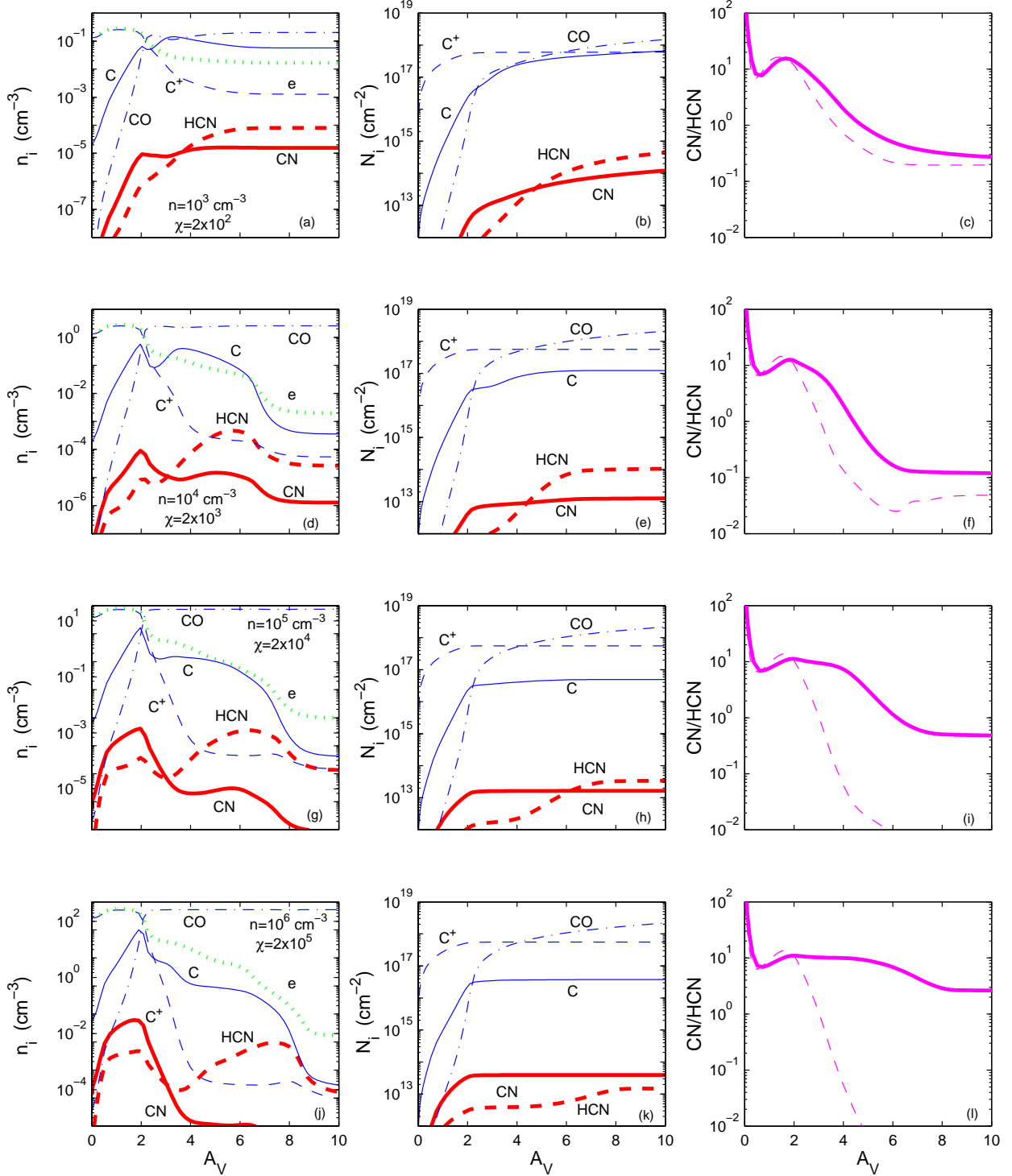


Fig. 5.— Model results for n equal to 10^3 , 10^4 , 10^5 , and 10^6 cm^{-3} (from top to bottom) for constant ionization parameter $\chi/n = 0.2$ cm^3 . The cosmic-ray ionization rate $\zeta = 5 \times 10^{-17}$ s^{-1} in all four models. Displayed profiles are for C^+ , C , CO , CN , HCN , and electrons, as functions of A_V . The lefthand panels display the volume densities. The middle panels show the integrated column densities. The righthand panels show the volume (dashed) and column (solid) CN/HCN density ratios. The second row, with $n = 10^4$ cm^{-3} , $\chi = 2 \times 10^3$ is our “reference model”.

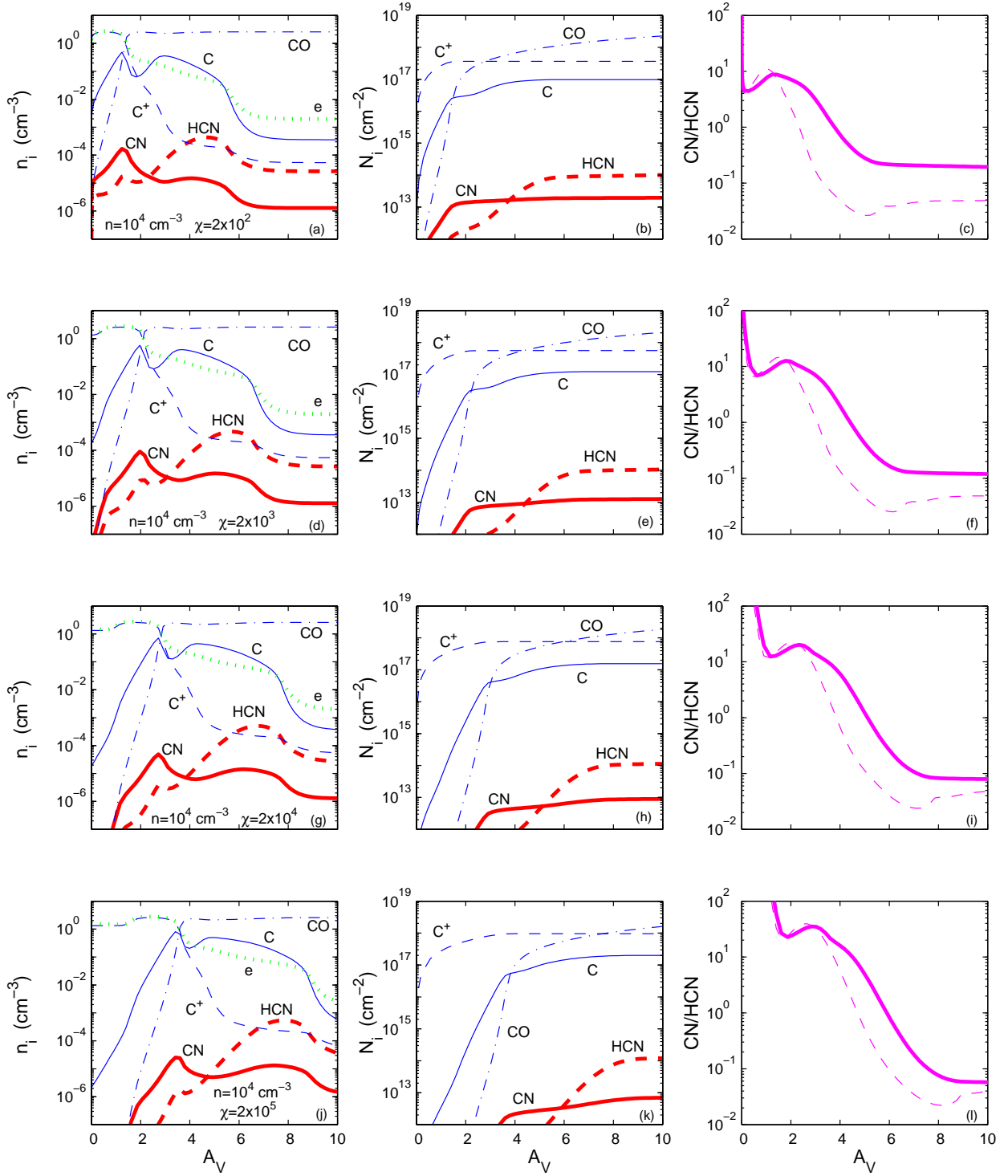


Fig. 6.— Model results for $n = 10^4 \text{ cm}^{-3}$, and χ equal to 2×10^2 , 2×10^3 , 2×10^4 , and $2 \times 10^5 \text{ cm}^{-3}$, and $\zeta = 5 \times 10^{-17} \text{ s}^{-1}$. The second row is our reference model.

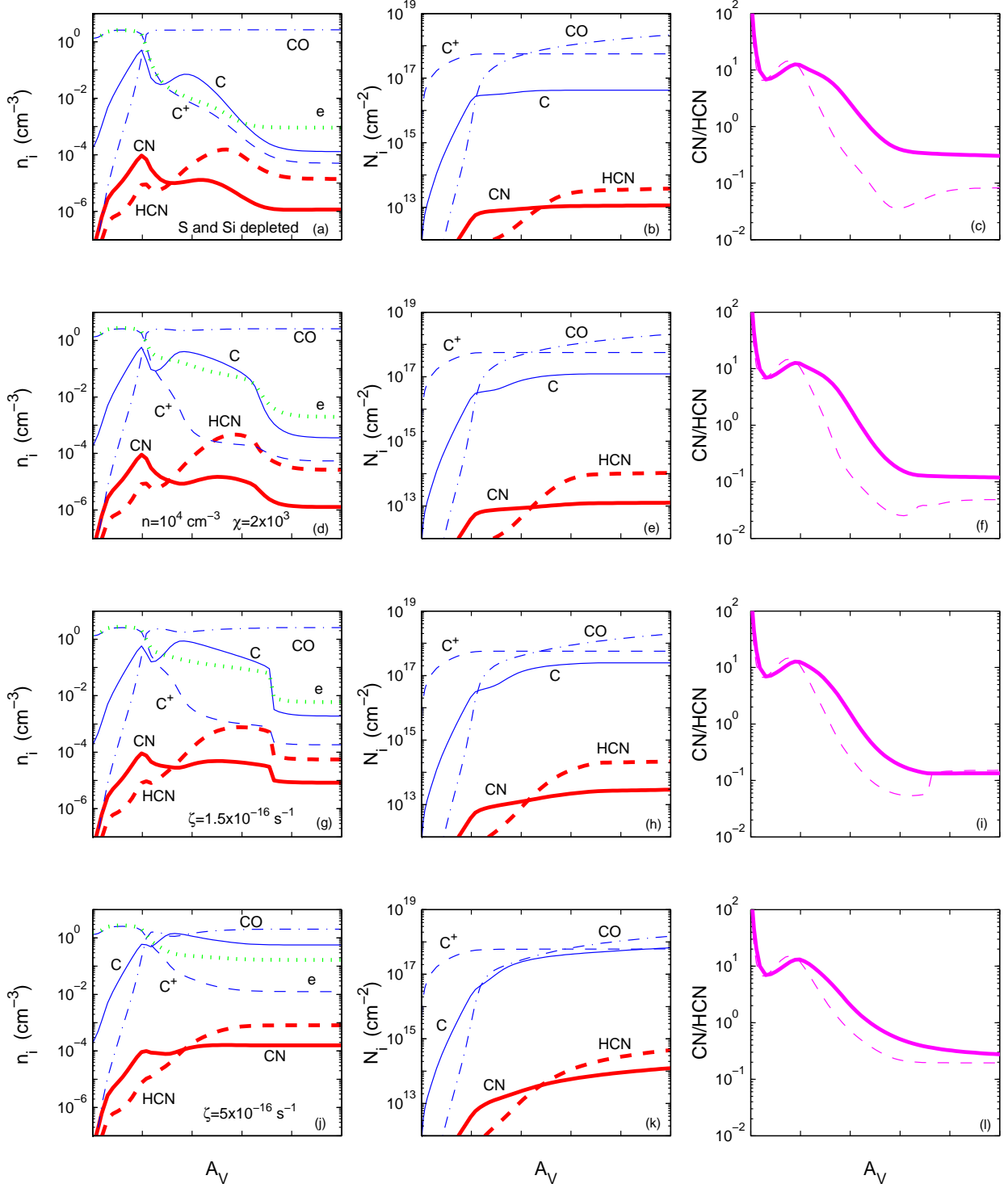


Fig. 7.— Results for $n = 10^4 \text{ cm}^{-3}$, and $\chi = 2 \times 10^3$. In the upper row the gas phase abundances of S and Si are reduced by a factor of 100. The second row is our reference model, with standard abundances and $\zeta = 5 \times 10^{-17} \text{ s}^{-1}$. In the third and fourth rows, ζ is increased to 1.5×10^{-16} and $5 \times 10^{-16} \text{ s}^{-1}$.

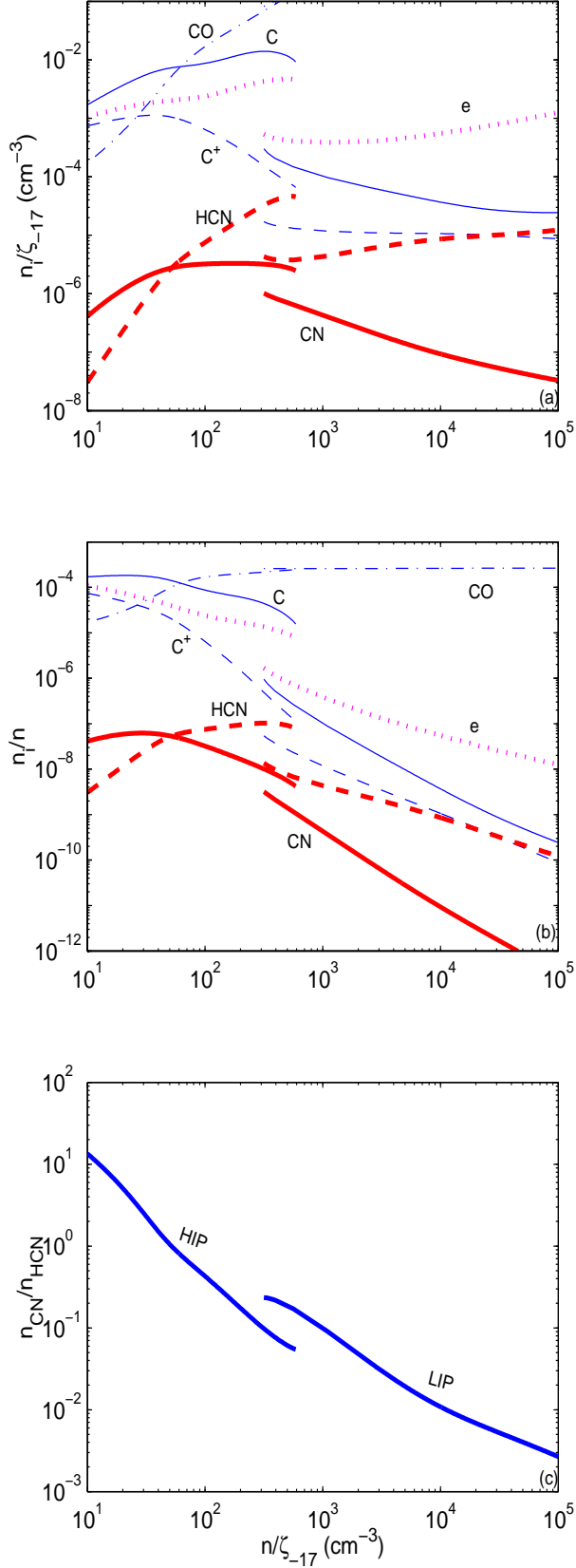


Fig. 8.— Densities of CN, HCN, C⁺, C, CO, and electrons, in the cosmic-ray dominated cores, showing the high and low ionization phases. Panels (a) and (b) show the densities n_i/ζ_{-17} and density fractions n_i/n , as functions of n/ζ_{-17} , where ζ_{-17} is the cosmic-ray